IEEE Access
Multidisciplinary ⋮ Rapid Review ⋮ Open Access Journal

Received July 14, 2021, accepted August 29, 2021, date of publication September 10, 2021, date of current version October 13, 2021.

Digital Object Identifier 10.1109/ACCESS.2021.3111852

Dynamic Disturbance Analysis of Whiskbroom Area Array Imaging of Aerospace Optical Camera

SHAOEN WANG, XIUBIN YANG, RUPENG FENG, SUINING GAO, AND JINLIANG HAN

Changchun Institute of Optics, Fine Mechanics and Physics, Chinese Academy of Sciences, Changchun, Jilin 130033, China
Daheng College, University of Chinese Academy of Sciences, Beijing 100049, China
Key Laboratory of Space-Based Dynamic and Rapid Optical Imaging Technology, Chinese Academy of Sciences, Changchun, Jilin 130033, China

Corresponding author: Xiubin Yang (yangxiubin@ciomp.ac.cn)

This work was supported in part by the National Natural Science Foundation of China (NSFC) under Grant 62171430 and Grant 62101071, in part by the Natural Science Foundation of Jilin Province under Grant 202512JC010280218, and in part by the Innovation and Entrepreneurship Team Project of Zhuhai City under Grant ZH0405190001PWC.

ABSTRACT The whiskbroom scanning imaging mode effectively expands the imaging field of the space optical camera, and realizes high-resolution and wide-width spatial imaging. However, the dynamic disturbance in the short-term and large-scale imaging process will cause uneven degradation of the image. Therefore, a geometric model of the camera instantaneous imaging at a moment is constructed. Then, the movement trend of the camera and the deflection of the light are deduced separately for establishing the analysis model of the kinematic disturbance and the morphological disturbance. Finally, the dynamic disturbance result of the imaging process is obtained by fusing both kinematic disturbance and morphological disturbance, and the simulated image of the dynamic disturbance is evaluated by combining the geometric parameters and the image quality evaluation index. The results show that the dynamic disturbance of the imaging will be enhanced with the increase of the whiskbroom angle and angular velocity, resulting in the decrease of the peak signal-to-noise ratio and the structural similarity of the image. When the angular velocity on the 500km orbit increases from $1°/s$ to $10°/s$, the peak signal-to-noise ratio and structural similarity of the simulated image, affected by the combining influence of kinematic disturbance and morphological disturbance, decrease by 2.1454 dB and 0.1131 respectively at 0°, but decrease by 1.5680 dB and 0.0405 at 45°. The analysis results of this paper can provide an effective reference for further research on the degradation process of whiskbroom ultra-wide image and improve the quality of the image.

INDEX TERMS Atmospheric optical properties, dynamic disturbance, image degradation, image simulation, optical path calculation.

I. INTRODUCTION

Space optical remote sensing technology appears actively in crucial fields such as information detection and situational awareness, and gradually becomes an efficient and indispensable means of obtaining information in modern society. Because of the lack of imaging and control technology, the static push-broom mainly used in the early age usually led to insufficient regional coverage and resolution capabilities of cameras, which reduced the imaging efficiency and orbital resource utilization [1]. The multi-camera image stitching technology used to enrich the imaging coverage also further reduces the image resolution, aggravating the image quality degradation [2], [3]. For this reason, dynamic analysis is proposed to apply to the whiskbroom process, which can effectively expand the imaging width and increase the area coverage through the whiskbroom scanning movement [4]. At the same time, single-camera imaging can also avoid the image degradation caused by the stitching process of multiple cameras, and satisfy the high-resolution and large-width imaging requirements of the optical remote sensing technology.

However, the kinematic characteristics of the whiskbroom scanning imaging process will introduce uneven dynamic disturbances and extend the imaging object distance of the camera, causing the optical path gradient of the imaging light in the transmission process, which will lead to the changing of resolution and the shifting of imaging area, and finally reduce the imaging quality. In the research of kinematic characteristics of whiskbroom scanning imaging, Xu [1] *et al.*

The associate editor coordinating the review of this manuscript and approving it for publication was Md Selim Habib.

proposed an inversion and recovery algorithm for whiskbroom scanning images by building a whiskbroom scanning model, and verified the rationality and feasibility of the model from the perspective of image restoration, realizing the geometric distortion correction of the whiskbroom imaging. Song *et al.* designed a dynamic frame imaging mode, verified the feasibility of the dynamic imaging mode can achieve large and wide imaging in terms of imaging mechanism. Zhao *et al.* proposed to analyze the velocity field in the dynamic process, established the vector field model of the motion velocity in the imaging process, and realized the imaging blur simulation and prediction of the complex motion state. Aiming at the degradation process of imaging light in the atmospheric environment, based on the Kolmogorov atmospheric turbulence model, Richard G. Lane [5], [6] respectively proposed two Kolmogorov phase screen simulation methods, and deduced the atmospheric degradation process from the spatial phase perspective. Starting from the point spread function, Zhang used the Huber norm regularization algorithm to estimate the point spread function of single-layer and multi-layer atmospheric turbulence, and established a new atmospheric turbulence phase calculation model, which improved the reliability of the phase calculation. Wu *et al.* invented a method that uses high-precision ultrasonic anemometer real-time sampling to obtain atmospheric temperature time series data, which achieved long-term continuous acquisition of accurate optical turbulence intensity. Dwivedi *et al.* studied the turbulence in the surface boundary layer through empirical methods, and verified the universality of the Kolmogorov model in calculating boundary turbulence. Based on the atmospheric refraction analysis model built by Noerdlinger [7] and others at the end of the last century, Yan [8], Wang [9] and Gao [10] and others combined line-of-sight vector tracing, rational polynomial coefficients, LOWTRAN7's ray tracing model, which improves the atmospheric refraction model, then constructed different layered atmospheric analysis models and calculated the corresponding atmospheric refraction offset size, and finally analyzed the geometric principle of atmospheric offset from the geometric angle of ray tracing. However, due to the quasi-stationary nature of the imaging model, without considering the impact of the dynamic disturbance caused by the movement of camera whiskbroom, the above-mentioned scholars all used the static imaging model. In addition, there is a lack of simulation and discussion of imaging results in the correction research of geometric positioning.

Therefore, for obtaining the kinematic disturbances during the whiskbroom scanning process, this paper firstly calculates the disturbance distribution of image displacement under the whiskbroom motion, according to the kinematic model of the whiskbroom scanning imaging. Then, based on the characteristics of the near-ground atmospheric environment, a near-ground atmospheric environment model for imaging light transmission is constructed to derive the morphological disturbance of the gradual optical path gradient. Finally, with calculating the quality evaluation parameters of the whiskbroom images under different conditions obtained by simulation, the image quality evaluation under different dynamic disturbances can be obtained.

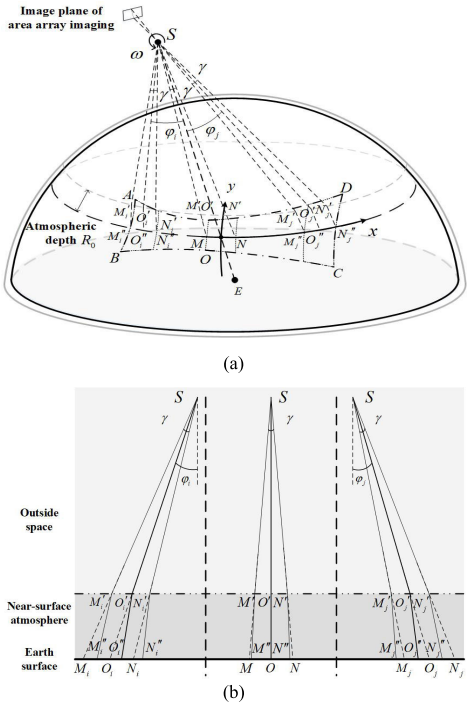

FIGURE 1. Principle of light transmission in whiskbroom scan imaging: (a) schematic diagram of whiskbroom scanning imaging process, (b) The transmission process of imaging light at different whiskbroom angles.

II. ANALYSIS OF THE WHISKBROOM IMAGING PROCESS OF AEROSPACE OPTICAL CAMERA

A. THE INVERSION PROCESS OF WHISKBROOM IMAGING

Compared with the static push-broom imaging mode, the whiskbroom scanning imaging with high dynamic characteristics greatly improves the maneuverability of the space optical camera and realizes the expansion of imaging coverage in a short time. However, the rapidly changing of objective distance also causes the change of the optical path in the atmospheric space, which leads to the deviation of the light and the degradation of the image quality.

Fig.1. (a) shows the whiskbroom scanning imaging process of the aerospace optical camera. Under influence of the earth curvature and the change of the imaging object distance, the total coverage area *ABCD* of the actual imaging is a pincushion area with wide ends and narrow center. When the camera carries out area array imaging, the wider sides of the imaging coverage area will produce compression in the output image, resulting in image distortion and a decrease in ground resolution. Fig.1. (b) shows the transmission process of imaging light under atmospheric environment. When the whiskbroom angle is φ and the field of view of single pixel is γ, the light will gradually change from $M'M''$ to $N'N''$ due to the effect which combined with the whiskbroom angle and the refractive index, resulting in the ground resolution to change from MN to $M''N''$.

Based on the characteristics of the whiskbroom scanning imaging process, the existing dynamic disturbance is divided

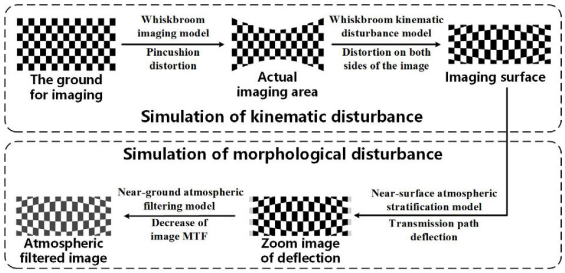

FIGURE 2. Inversion of degradation process in whiskbroom imaging.

into two parts: kinematic disturbance and morphological disturbance. The analysis process is shown in Fig.2. In the analysis of kinematic disturbance, the whiskbroom geometric model and the migration simulation model is constructed according to the image-shift in imaging area. In the morphological disturbance analysis, the near-ground light transmission model is constructed as well, according to the light path gradient. Finally, the kinematic disturbance and the morphological disturbance are combined to realize the dynamic disturbance analysis of the whiskbroom scanning imaging.

B. ANALYSIS OF MOTION DISTURBANCE IN WHISKBROOM IMAGING

1) CONSTRUCTION OF WHISKBROOM MODEL

In order to simplify the analysis of the whole whiskbroom scanning process, consulting with calculus algorithm, the whole imaging process can be described as the superimposition of the instantaneous imaging results. Select the moment when the whiskbroom angle is φ in Fig.1. (a) to construct the instantaneous model of imaging as shown in Fig.3, where the area $A'B'C'D'$ is the imaging region. During the whiskbroom scanning process, the objective distance SO' will change with φ, which causes the change of the instantaneous imaging region $A'B'C'D'$, and finally lead to the actual imaging region $ABCD$ showing in a pillow shaped. When the variation range of whiskbroom angle is $[-\varphi_0, \varphi_0]$, and the variation range of the FOV corresponding to each pixel along the orbit is $[-\beta_0, \beta_0]$, S_{ABCD} and $S_{A'B'C'D'}$ respectively represent the whole imaging region and the instantaneous imaging region at φ. According to the geometric model shown in Fig.3, the following can be obtained:

$$\begin{aligned} S_{ABCD} &= \int_{-\varphi_0}^{\varphi_0} S_{A'B'C'D'}(\varphi)\, d\varphi \\ &= \int_{-\varphi_0}^{\varphi_0} \int_{-\beta_0}^{\beta_0} \frac{H^2 \tan\beta \sin\gamma}{\cos^3\varphi} d\beta d\varphi \end{aligned} \tag{1}$$

During the imaging process, the ground coordinate system is constructed as follows: the sub-satellite point O is taken as the origin of the coordinate system, the direction perpendicular to orbit is x direction, and the direction along orbit is y direction. According to the motion characteristics of the camera, the ground trajectory of the imaging point I on the ground, which is composed of pixel i with field angle β_0, can be written as:

$$y = \sqrt{x^2 + H^2} \cdot \tan\beta_0 \tag{2}$$

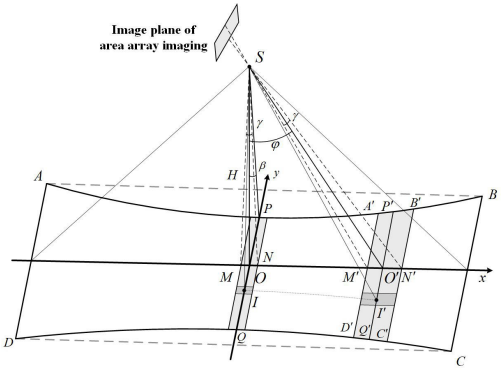

FIGURE 3. Instantaneous model study of whiskbroom scanning imaging.

Combined with (2) and the characteristics of whiskbroom scanning process, with the constant change of φ, the instantaneous imaging region $A'B'C'D'$ will also produce different distortion processes in the vertical and along the orbit directions of the camera, resulting in a two-dimensional degradation process in the imaging region.

2) DISTORTION ANALYSIS OF IMAGING AREA

According to the characteristics of the imaging mode, the strip width $M'N'$ in the direction of vertical orbit of $A'B'C'D'$ in the instantaneous imaging region, and the field angle γ corresponding to the unit pixel in the whiskbroom scanning process is defined as $\gamma = a/f$. As the instantaneous model shown in Fig.3, when the whiskbroom angle is φ, the position of the midpoint M' in the camera's instantaneous imaging region $A'B'C'D'$ in the ground coordinate system x_φ is:

$$x_\varphi = \sum_{n=0}^{n=\varphi/\gamma} \left(H \cdot \left(\tan\left(n\gamma + \gamma/2\right) - \tan\left(n\gamma - \gamma/2\right)\right)\right) \tag{3}$$

In this case, $M'N'$ corresponding to unit pixel is:

$$M'N' = H \cdot \left(\tan\left(\varphi + \gamma/2\right) - \tan\left(\varphi - \gamma/2\right)\right) \tag{4}$$

For (3) and (4), the nonlinear growth feature of the tangent function makes $M'N'$ have different calculation results at different whiskbroom angles, and the size of $M'N'$ also increases with the increase of whiskbroom angles. When the whiskbroom angle is 0°, the width of the strip MN in the imaging region of the sub-satellite point is the resolution of the aerospace optical camera:

$$M'N' = H \cdot \left(\tan\left(\varphi + \gamma/2\right) - \tan\left(\varphi - \gamma/2\right)\right) \tag{5}$$

Although $M'N'$ is not the same at different whiskbroom angles, in the actual imaging plane, $M'N'$ in all instantaneous imaging regions is reflected in the same pixel size. As a result, the coverage of both sides of the image in the vertical track direction is increased, the ground resolution is reduced, and image distortion is introduced.

It is same as the analysis of the vertical orbit direction, the imaging width $P'Q'$ along the orbit direction of the instantaneous imaging region $A'B'C'D'$ is selected as the analysis object. a and f represent the pixel size and focal length of the

camera respectively, and N represents the number of pixels on the area array imaging plane. Then, the field of view angle β_i between pixel i with n pixels interval from the midpoint S of the area array imaging plane and the optical axis of the sub-satellite point can be written as $\beta_i = na/f$. When the whiskbroom angle is φ, the abscissa x_φ of P' and Q' in the ground coordinate system of the instantaneous imaging region $A'B'C'D'$ can be calculated according to (2), and the width $P'Q'$ of $A'B'C'D'$ can be calculated as follows:

$$P'Q' = 2y_\varphi = 2\sum_{n=0}^{n=N/2}\sqrt{x_\varphi^2 + H^2}\cdot\tan\left(\frac{na}{f}\right) \tag{6}$$

Substituting the calculation formula of ground coordinate system x_φ in (3) into (6), the final expression of $P'Q'$ can be obtained as follows:

$$P'Q' = 2\sum_{n=0}^{n=N/2}\sqrt{\sum_{n=0}^{n=\varphi/\gamma}\left(H\cdot\left(\tan\left(n\gamma+\gamma/2\right)-\tan\left(n\gamma-\gamma/2\right)\right)\right)^2+H^2}\cdot\tan\left(\frac{na}{f}\right) \tag{7}$$

By analogy with the degradation analysis in the direction of vertical rail, the instantaneous imaging region $A'B'C'D'$ is reflected in n pixels in the actual imaging plane. With the increase of the swing angle, the coverage width of the imaging image along the orbit direction increases, which will also lead to the distortion of the image, reduce the resolution ability of the camera and cause image degradation.

(7) reflects the overall degradation relationship in the two-dimensional direction of the ground in the actual imaging process. Thus, degradation analysis and simulation model construction of the whole process can be completed by changing the whiskbroom angle φ and the number of pixels N of the detector.

3) SIMULATION OF IMAGE SHIFT IN IMAGING AREA

During the imaging process, the actual recording on the image surface of the camera is the sum of all images during the exposure time, that is, the data recorded in each pixel unit is the average gray level information during the exposure time. According to this characteristic, the velocity vector distribution of whiskbroom scanning process as shown in Fig. 4, based on Fig. 3, can be constructed for simulating the kinematic disturbance existing in the imaging region.

When the exposure time is Δt, the total velocity of the ground area corresponding to a pixel on the image plane is $\boldsymbol{V}$. According to the imaging model, when the earth radius is R and the camera orbit height is H, then the offset $\boldsymbol{C}$ of the ground area can be written as

$$\boldsymbol{C} = \boldsymbol{V}\cdot\Delta t = (\boldsymbol{v}_e + \boldsymbol{v}_o + \boldsymbol{v}_t) = \left(\boldsymbol{\omega}_e\cdot R\cdot\cos\alpha + \boldsymbol{V}_o\cdot\frac{R}{R+H} + \boldsymbol{\omega}_o\cdot\frac{H}{\cos\varphi_i\cdot\cos\beta_i}\right)\cdot\Delta t \tag{8}$$

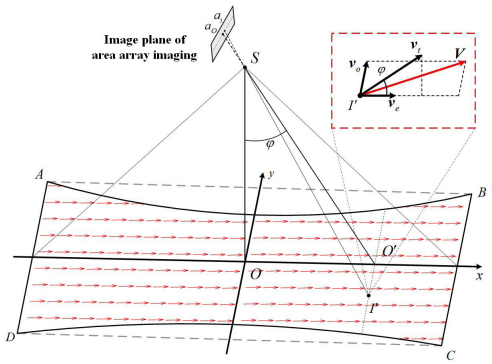

FIGURE 4. Velocity vector sketch of whiskbroom imaging.

where $\boldsymbol{v}_e$ is the ground velocity produced by the rotation of the earth, $\boldsymbol{\omega}_e$ is the angular velocity of the earth's rotation, α is the latitude of the ground area; $\boldsymbol{V}_o$ is the orbital velocity of the camera, $\boldsymbol{v}_o$ is the projection velocity of the camera's orbital velocity on the ground; $\boldsymbol{v}_t$ is the offset velocity generated by the whiskbroom movement, and $\boldsymbol{\omega}_o$ is the angular velocity of the whiskbroom angle. M represents the gray value recorded on the pixel unit:

$$M = \frac{\sum_{i=1}^{n} d_i\cdot M_i}{\sum_{i=1}^{n} d_i} \tag{9}$$

where, M_i and d_i represent the gray value of the ground area passed by the offset path and its distance weight, respectively. The distance weight of the ground area closer to the offset path is heavier than other areas.

C. ANALYSIS OF DISTURBANCE IN THE ATMOSPHERIC ENVIRONMENT

The main reason for the morphology disturbance of environment is the unevenly distributed refractive index in the atmosphere near the earth. According to empirical formulas and previous studies [7]–[10], the value of atmospheric refractive index n is related to factors such as atmospheric pressure P, atmospheric temperature T, and incident light wavelength λ. Among them, atmospheric pressure P and atmospheric temperature T are also functions of atmospheric altitude h, as follows:

$$\begin{aligned}(n-1)\times 10^8 &= \left(2371.34 + \frac{683939.7\lambda^2}{130\lambda^2-1} + \frac{4547.3\lambda^2}{38.9\lambda^2-1}\right)\\ &\quad\times D_1\left(P\left(h\right), T\left(h\right)\right)\\ &\quad+\left(6487.31+\frac{58.058}{\lambda^2}-\frac{0.7115}{\lambda^4}+\frac{0.08851}{\lambda^6}\right)\\ &\quad\times D_2\left(P\left(h\right), T\left(h\right)\right)\end{aligned} \tag{10}$$

According to the calculation result of (10), the atmospheric refractive index can be divided into three parts: When the altitude near the ground is lower than 11km, the atmospheric environment is in the troposphere, where the atmospheric refractive index changes relatively sharply with altitude, and

the refractive index decreases with the increase in altitude. When the altitude is between 11km and 47.5km, the atmospheric environment enters the stratosphere, and the decline rate of the refractive index gradually tends to be gentle. Until the altitude reaches 47.5km and above, the atmospheric refractive index tends to be constant with a value of 1. Therefore, based on the boundary between the troposphere and the stratosphere at 11km, a two-layer atmospheric model including all the troposphere and part of the stratosphere is constructed to complete the analysis of atmospheric environmental disturbances.

1) TRANSMISSION DEFLECTION OF IMAGING LIGHT

In order to improve the calculation accuracy of the optical path of the imaging light, the existing double-layer atmosphere model needs to be further refined. For achieving further refinement of the atmosphere model, the upper and lower layers of the double-layer atmosphere model are separated at intervals of 500m and 100m respectively.

Similarly, the moment when the instantaneous whiskbroom angle of the optical camera is φ, is selected to present the theoretical model of the instantaneous transmission path of the optical camera, as shown in Fig.5. (a). In the figure, E is the center of the earth; S is the optical camera; Point P is the incident point of imaging light outside the atmospheric model; B and A represent the ground imaging points with or without morphological disturbance; H and R represent the orbital height and earth radius respectively. The transmission process of imaging light in the i atmospheric sublayer is shown in Fig.5. (b). The refractive index n_i can be expressed by the arithmetic mean of the refractive indexes of $O_{(i-1)i}$ and $O_{i(i+1)}$, which is $n_i = (n_{O_{(i-1)i}} + n_{O_{i(i+1)}})/2$. $|L_i| = O_{(i-1)i}O_{i(i+1)}$ represents the transmission distance of imaging light in the i layer, R_{i-1} and R_i are the height of the upper and lower boundary of the i layer from the ground respectively. The $\theta_i = \angle O_{(i-1)i}EO_{i(i+1)}$ represents the angle of the center of the earth of $|L_i|$. According to the geometric principle, we can get:

$$\begin{aligned} \theta_i &= \psi_{(i+1)i} - \psi_{it} \\ \frac{R+R_{i-1}}{\sin\psi_{(i+1)i}} &= \frac{R+R_i}{\sin\psi_{it}} = \frac{|L_i|}{\sin\theta_i} \end{aligned} \tag{11}$$

According to Snell's law, the total optical path PB of the imaging light in the near-ground atmosphere model is:

$$PB = \sum_{i=1}^{N} \frac{n_i^2(R+R_i)\sin\left(\arcsin\left(\frac{R+R_{i-1}}{R+R_i}\sin\psi_{ii}\right) - \arcsin\left(\frac{n_{i-1}\sin\psi_{ii}}{n_i}\right)\right)}{n_{i-1}\sin\psi_{ii}} \tag{12}$$

Similarly, when the whiskbroom angle is φ, the offset $|AB|$ of the imaging light on the ground due to deflection is:

$$|AB| = R \cdot \left(\left(\arcsin\left(\frac{R+H}{R}\sin\varphi\right) - \varphi\right)\right.$$

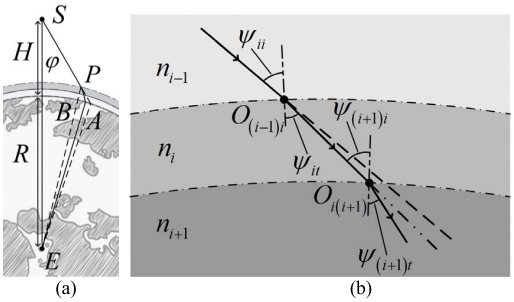

FIGURE 5. (a) Geometrical principles of instantaneous transmission path. (b) Transmission process of imaging light in layer i.

$$\left. - \sum_{i=1}^{N} \left(\arcsin\left(\frac{n_{i-1}\,(R+R_{i-1})\sin\psi_{ii}}{n_i\,(R+R_i)}\right) - \arcsin\left(\frac{n_{i-1}\sin\psi_{ii}}{n_i}\right)\right)\right) \tag{13}$$

(13) reflects the instantaneous ground offset of the imaging light when the whiskbroom angle is φ. Combining with (3), the corrected coordinate $x'_\varphi = x_\varphi - |AB|$ under the deflection degradation of the near-ground atmospheric environment can be obtained to simulate the process of ground excursions and degradation of the imaging light.

2) FILTERING DEGRADATION OF OPTICAL PATH GRADIENT

When the optical path distribution of the imaging light is determined, according to previous studies on atmospheric filtering [11]–[12], the degraded MTF produced by the near-ground atmospheric environment is:

$$\begin{aligned} MTF = \exp\left\{-57.53\,(f\nu)^{5/3}\,C_n^2\lambda^{1/3}R\left[1-0.5\left(\frac{f\nu\lambda}{D}\right)^{1/3}\right]\right\} \\ * \exp\left[-\frac{3.912}{R_m}\exp\left(-\frac{h}{1200}\right)R\right] \end{aligned} \tag{14}$$

where f is the focal length of the camera; ν is the spatial frequency; λ is the wavelength of the imaging light; R is the optical path size of the imaging light; D is the pupil diameter of the optical system; R_m is the visibility of the atmosphere near the ground; h is the altitude of the atmosphere; C_n^2 is the atmospheric refractive index structure constant, referring to the Kolmogorov atmospheric turbulence analysis model [13],

$$\begin{aligned} C_n^2(h) = {} & 5.94\times10^{-53}\cdot\left(v/27\right)^2 h^{10}e^{-h/1000} \\ & +2.7\times10^{-16}\cdot e^{-h/1500} + 1.7\times10^{-14}\cdot e^{-h/100} \end{aligned} \tag{15}$$

where, v represents the instantaneous wind speed in the atmospheric model when the altitude of the atmosphere is h, and $v = 21m/s$ is usually taken in the near-ground space [14]–[15]. According to (12), when the light transmission path structure near the ground is determined, the result of (12) is substituted into (14), which is:

$$MTF_\varphi = \prod_{i=1}^{N}\left\{\exp\left\{-57.53\,(f\nu)^{5/3}\,C_n^2\lambda^{1/3}L_i\left[1-0.5\left(\frac{f\nu\lambda}{D}\right)^{1/3}\right]\right\}\right.$$

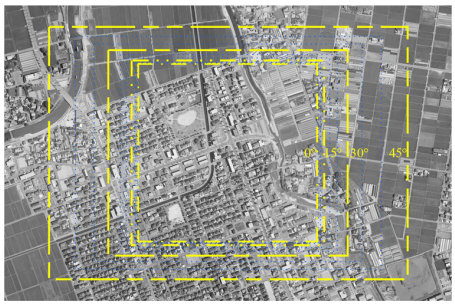

FIGURE 6. Comparison of imaging areas under different angles.

$$* \exp\left[-\frac{3.912}{R_m}\exp\left(-\frac{h}{1200}\right)R\right]\Bigg\} \tag{16}$$

According to (16), the morphological disturbances in different imaging environments can be calculated, and the corresponding degradation analysis simulation of the transmission environment can be realized.

III. SIMULATION AND RESULTS

In order to realize the dynamic disturbance analysis of the aerospace optical camera's whiskbroom scanning imaging, it is first necessary to establish the source of simulated image. Select $[-45°, 45°]$ as the range of the whiskbroom angle, the orbit height H is 500km, the earth radius R is 6400km, the focal length of the camera f is 500mm, the entrance pupil diameter D is 400mm, the pixel size a_0 is 1μm, the number of image pixels used in imaging is 1200×1200, and the imaging light wavelength λ is 550nm. Taking the 3000×2000-pixel image source as the standard ground imaging area, the image disturbance results under different conditions are simulated, according to the inversion process shown in Fig.2.

A. REFERENCE IMAGES UNDER DIFFERENT ANGLES

The center of the image source is set as the intersection of the camera's optical axis with the ground. Due to the symmetry of the range of whiskbroom angle, only the undisturbed images with the angle ranged of [0°,45°] are simulated, and the comparison of the imaging coverage of the reference images under different whiskbroom angles is shown in Fig. 6.

According to the imaging model shown in Fig.3, record the imaging parameters of the imaging coverage at 0°, 15°, 30°, and 45°, where the imaging area changes significantly in Fig.6. Taking the geometric mean GSD of the ground resolution GSD_x and GSD_y in the vertical and along the track directions to represent the ground resolution, $GSD = \sqrt{GSD_x^2 + GSD_y^2}$, the simulation results obtained are recorded in Table 1.

B. DISTURBANCE SIMULATION OF WHISKBROOM IMAGING

1) SIMULATION OF KINEMATIC DISTURBANCE

Taking the undisturbed images under different angles simulated in Fig.6 as the original images, specifying the camera exposure time as 1ms, the simulation results of the perturbation at the angular velocity from 1°/s to 10°/s are performed,

TABLE 1. Related imaging parameters under different side swing angles.

	0°	15°	30°	45°
Width of the vertical rail (km)	1.1990	1.2851	1.5987	2.3980
Minimum width along the rail(km)	1.2000	1.2423	1.3856	1.6971
Maximum width along the rail (km)	1.2000	1.2427	1.3866	1.6991
Width difference along the rail (m)	0.0000	0.4005	0.9617	2.0401
Coverage area of imaging (km^2)	1.4388	1.5967	2.2160	4.0720
Ground resolution of camera (m)	1.4142	1.4901	1.7638	2.4495

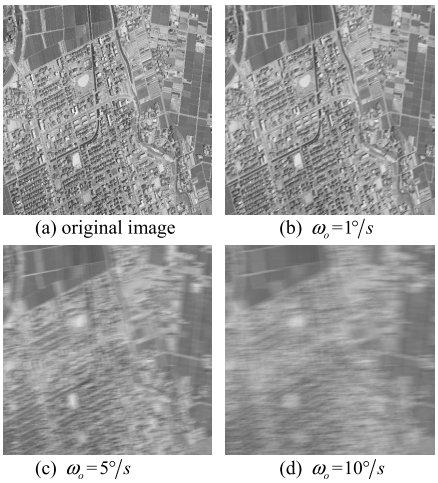

(a) original image (b) ω_o=1°/s (c) ω_o=5°/s (d) ω_o=10°/s

FIGURE 7. Image simulation at 45°.

TABLE 2. The peak signal-to-noise ratio of simulated images.

	1°/s	4°/s	7°/s	10°/s
0°	17.7816	16.1262	15.6242	15.4559
15°	17.8753	16.1620	15.6880	15.5337
30°	17.8137	16.1345	15.7818	15.6765
45°	17.9153	16.2715	16.0597	15.9524

and Fig.7 shows the original image and the simulated image of disturbance with angular velocity ω_o of 1°/s, 5°/s, and 10°/s at 45°.

Peak signal-to-noise ratio (PSNR) and structural similarity (SSIM) are commonly used to evaluate the imaging quality of remote sensing simulated images. PSNR represents the distortion of the simulated image, and SSIM represents the similarity between the simulated image and the original image. The larger the PSNR value, the smaller the distortion of the simulated image, and the higher the image quality. The closer SSIM is to 1, the smaller the difference between the simulated image and the original image is, and the smaller the image degradation is. By evaluating the quality of the simulated image, we can get PSNR and SSIM under kinematic disturbance respectively, and the results are shown in Table 2 and Table 3.

2) SIMULATION OF MORPHOLOGICAL DISTURBANCE

Taking the undisturbed images at different angles simulated in Fig.6 as the original image, according to the symmetry of

TABLE 3. The structural similarity of simulated images.

	$1°/s$	$4°/s$	$7°/s$	$10°/s$
0°	0.3988	0.3198	0.2816	0.2750
15°	0.4000	0.3112	0.2783	0.2713
30°	0.4043	0.2822	0.2621	0.2568
45°	0.4229	0.2778	0.2649	0.2607

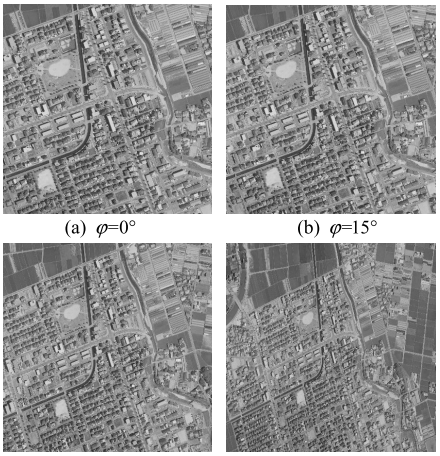

(a) φ=0° (b) φ=15° (c) φ=30° (d) φ=45°

FIGURE 8. Morphological disturbance simulation of whiskbroom imaging.

TABLE 4. Imaging parameters under different angles.

	0°	15°	30°	45°
Minimum deflection (km)	0.0000	0.7604	2.1761	6.7467
Maximum deflection (km)	0.0031	0.7689	2.1964	6.8304
Degradation MTF	0.9121	0.9086	0.8965	0.8673
PSNR (dB)	22.6268	20.8468	16.4205	14.8065
SSIM	0.8672	0.7447	0.3230	0.1902

TABLE 5. PSNR of joint disturbance simulated images.

	$1°/s$	$4°/s$	$7°/s$	$10°/s$
0°	17.2812	15.8189	15.3128	15.1358
15°	17.4289	15.9209	15.3909	15.2058
30°	17.2137	15.9522	15.4577	15.2828
45°	16.7607	15.7621	15.3720	15.1927

the whiskbroom range, it can be seen that the morphological disturbances generated on both sides are the same. Similarly, select the angles at 0°, 15°, 30°, and 45° to simulate morphological disturbances. The results are shown in Fig.8 and the relevant data are recorded in Table 4.

3) JOINT DISTURBANCE SIMULATION

Select the simulated image obtained in Fig. 6 as the initial image, simulate the kinematic disturbance and morphological disturbance that existing during the whiskbroom scanning process, and finally record the PSNR and SSIM of the final simulated image with angles at 0°, 15°, 30° and 45° in Table 5 and Table 6. Fig.9 shows the corresponding simulated images when the whiskbroom angle is 0° and 45°, and the angular velocity is $1°/s$ and $10°/s$.

C. SIMULATION RESULTS AND ANALYSIS

According to the representative simulated images shown in Fig.6 to Fig.9, when imaging disturbances are not

TABLE 6. SSIM of joint disturbance simulated images.

	$1°/s$	$4°/s$	$7°/s$	$10°/s$
0°	0.3931	0.3314	0.2885	0.2800
15°	0.3934	0.3345	0.2915	0.2806
30°	0.3359	0.3152	0.2815	0.2705
45°	0.3126	0.3055	0.2812	0.2721

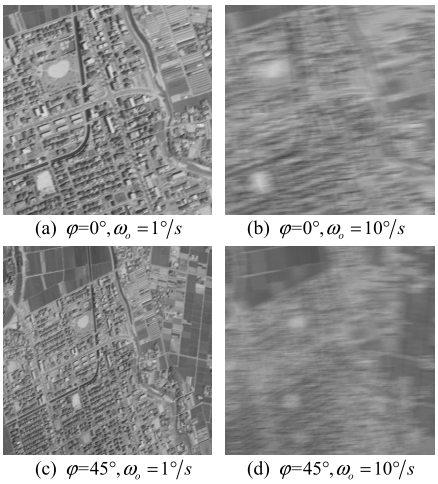

(a) φ=0°, $\omega_o = 1°/s$ (b) φ=0°, $\omega_o = 10°/s$ (c) φ=45°, $\omega_o = 1°/s$ (d) φ=45°, $\omega_o = 10°/s$

FIGURE 9. Joint disturbance simulation of whiskbroom scanning imaging.

considered, the imaging coverage will increase significantly with the increase of the whiskbroom angle, causing a decrease in imaging accuracy.

Different from kinematic disturbance, the morphological disturbance of the imaging environment is greatly affected by the change of the whiskbroom angle. The larger the whiskbroom angle is, the greater the morphological disturbance becomes. When the whiskbroom angular velocity is increased to $10°/s$ and the angle is 0° and 45°, the PSNR under the influence of kinematic disturbance is 15.4559 dB and 15.9524 dB, the SSIM is 0.2750 and 0.2607 respectively. While the PSNR under the influence of joint disturbance is 15.1358 dB and 15.1927 dB, the SSIM is 0.2800 and 0.2721.

The simulation results show that the whiskbroom scanning imaging mode of the aerospace optical camera effectively increases the coverage area, but reduces the ground resolution at the same time, resulting in a certain imaging distortion in results and leading to a decrease in image quality. The kinematic disturbance and morphological disturbance of the camera will also affect the image quality from different aspects. According to the image evaluation index based on PSNR and SSIM, it can be seen that the kinematic disturbance of the camera is still the most important factor for the deterioration of the image quality.

IV. CONCLUSION

Based on the whiskbroom scanning imaging theory of aerospace optical cameras, this paper synthesized the near-ground double-layer atmosphere model, constructed an imaging degradation analysis model under the influence of camera motion disturbance and imaging environment disturbance during whiskbroom scanning, and simulated the degraded images under different disturbance conditions in the

whiskbroom scanning imaging mode. At last, the evaluation and analysis of the degraded images are completed. In the imaging process, the kinematic disturbance generated by the camera's whiskbroom is the main reason for the image quality degradation, and the imaging parameters of the aerospace optical camera have obvious symmetrical distribution relatively to the sub-satellite point trajectory. In addition, with the increase of the whiskbroom angle, the coverage area increases, the ground resolution ability decreases, and the disturbance of the imaging environment increases. All of the above will further reduce the imaging quality of the camera. Therefore, it is necessary to prioritize restrictions on the motion state of the whiskbroom motion under the premise of satisfying the imaging width in order to obtain high-quality imaging results.

REFERENCES

[1] C. Xu, G. Jin, X. Yang, T. Xu, and L. Chang, "Inversion restoring algorithm for whiskbroom scanning images synthesized with deep convolutional neural network," *Acta Optica Sinica*, vol. 39, no. 12, 2019, Art. no. 1228001.
[2] X. Liu, Z. Tian, W. Yan, and X. Duan, "KW-SIFT descriptor for remote-sensing image registration," *Chin. Opt. Lett.*, vol. 9, no. 6, pp. 061001–61005, 2011.
[3] R. Bouchiha and K. Besbes, "Comparison of local descriptors for automatic remote sensing image registration," *Signal, Image Video Process.*, vol. 9, no. 2, pp. 463–469, Feb. 2015.
[4] Q. Yue, Z. Qiu, and Y. Jia, "Impact of TDI CCD camera dynamic imaging on geometric quality by mathematic simulation," *Sci. Surv. Mapping*, vol. 37, no. 3, pp. 14–17, 2012.
[5] R. G. Lane, A. Glindemann, and J. C. Dainty, "Simulation of a Kolmogorov phase screen," *Waves Random Media*, vol. 2, no. 3, pp. 209–224, Jul. 1992.
[6] C. M. Harding, R. A. Johnston, and R. G. Lane, "Fast simulation of a Kolmogorov phase screen," *Appl. Opt.*, vol. 38, no. 11, pp. 2161–2170, Apr. 1999.
[7] P. D. Noerdlinger, "Atmospheric refraction effects in earth remote sensing," *ISPRS J. Photogramm. Remote Sens.*, vol. 54, nos. 5–6, pp. 360–373, Dec. 1999.
[8] M. Yan, C. Wang, J. Ma, Z. Wang, and B. Yu, "Correction of atmospheric refraction geolocation error for high resolution optical satellite pushbroom images," *Photogramm. Eng. Remote Sens.*, vol. 82, no. 6, pp. 427–435, Jun. 2016.
[9] Y. Wang, Y. Zhu, M. Wang, S. Jin, and Q. Rao, "Atmospheric refraction calibration of geometric positioning for optical remote sensing satellite," *IEEE Geosci. Remote Sens. Lett.*, vol. 17, no. 12, pp. 2130–2134, Dec. 2020.
[10] B. C. Gao, E. Ward, J. Bowles, and A. Yingling, "A systematic sensitivity study on surface pixel shifts in high spatial resolution satellite images resulting from atmospheric refraction in the sensor to surface ray path," *Sensors*, vol. 20, no. 23, Dec. 2020, Art. no. 6874.
[11] J. Chao, G. Zexun, and C. Qing, "Removed atmospheric degradation of remote-sensing images combined with meteorologic model," *J. Geomatics Spatial Inf. Technol.*, vol. 38, no. 9, pp. 9–11 and 16, 2015.
[12] P. W. Hawkes, "Statistical optics," *Nature*, vol. 316, no. 6029, pp. 584–585, 1985.
[13] L.-Y. Cui, B.-D. Xue, X.-G. Cao, J.-K. Dong, and J.-N. Wang, "Generalized atmospheric turbulence MTF for wave propagating through non-Kolmogorov turbulence," *Opt. Exp.*, vol. 18, no. 20, pp. 21269–21283, Sep. 2010.
[14] X. W. Huang, Y. F. Bai, and X. Q. Fu, "Image transmission with binary coding for free space optical communications in the presence of atmospheric turbulence," *Appl. Opt.*, vol. 59, no. 33, pp. 10283–10288, Nov. 2020.
[15] M. Yan, Z. Y. Wang, C. Y. Wang, and B. Y. Yu, "Atmosphere refraction effects in object locating for optical satellite remote sensing images," *Acta Geodaetica et Cartographica Sinica*, vol. 44, no. 9, pp. 995–1002, Sep. 2015.

SHAOEN WANG received the B.S. degree from Harbin Institute of Technology, Weihai, China, in 2019. He is currently pursuing the Ph.D. degree with Changchun Institute of Optics, Fine Mechanics, and Physics, Chinese Academy of Sciences. His research interests include dynamic imaging and image processing.

XIUBIN YANG received the B.S. degree in physics from Nankai University, Tianjin, in 2006, and the Ph.D. degree in optical engineering from Chinese Academy of Sciences, Changchun, in 2011. He is currently a Professor with the Department of Space New Technique, Changchun Institute of Optics, Fine Mechanics, and Physics, Chinese Academy of Sciences. His research interests include dynamic imaging process of space optical camera, new mode of optical imaging, and advanced optical payload technology.

RUPENG FENG received the master's degree from Xi'an University of Electronic Science and Technology, in 2013. He is currently working with Changchun Institute of Optics, Fine Mechanics, and Physics, Chinese Academy of Sciences. His main research interest includes design and application on spaceborne electronics product.

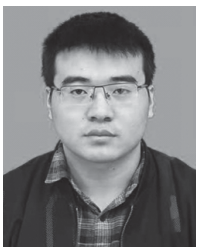

SUINING GAO received the B.S. degree from Nankai University, in 2020. He is currently pursuing the M.S. degree with Changchun Institute of Optics, Fine Mechanics, and Physics, Chinese Academy of Sciences. His main research interests include design of new multi-dimensional tensor optical systems and fusion image analysis based on deep learning.

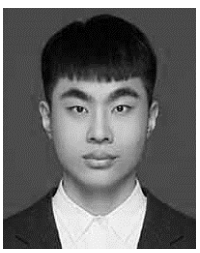

JINLIANG HAN received the B.Eng. degree in electronic information science and technology from Xiamen University, Xiamen, China, in 2018. He is currently pursuing the M.S. degree in optical engineering with Changchun Institute of Optics, Fine Mechanics, and Physics, Chinese Academy of Sciences. His research interests include dynamic optical imaging and super-resolution imaging.